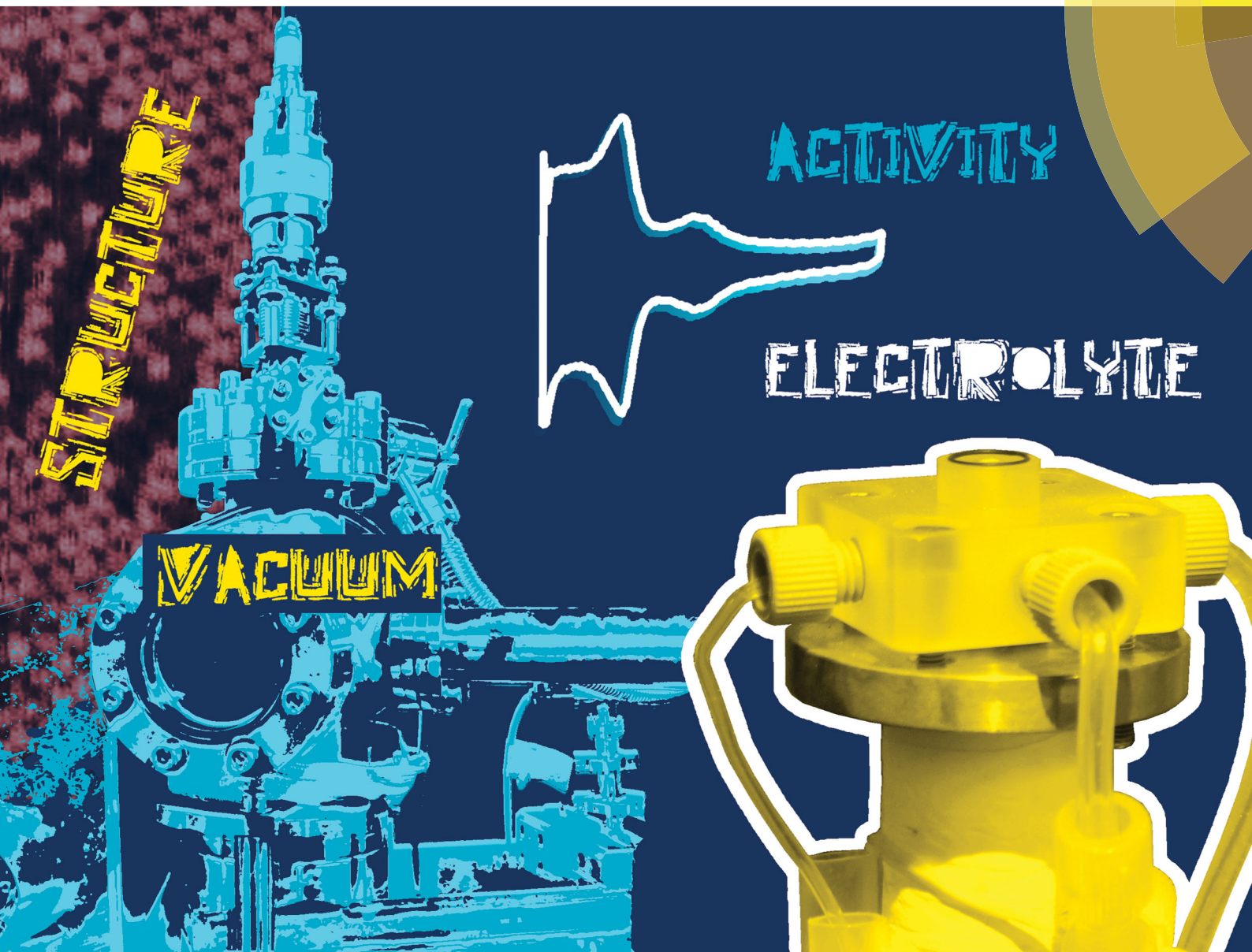


PCCP

Physical Chemistry Chemical Physics
rsc.li/pccp



ISSN 1463-9076



ROYAL SOCIETY
OF CHEMISTRY

PAPER

S. Brimaud, R. J. Behm et al.
A combined UHV-STM-flow cell set-up for
electrochemical/electrocatalytic studies of structurally
well-defined UHV prepared model electrodes



Cite this: *Phys. Chem. Chem. Phys.*,
2017, 19, 4166

A combined UHV-STM-flow cell set-up for electrochemical/electrocatalytic studies of structurally well-defined UHV prepared model electrodes†

J. Schnaitd,‡ S. Beckord, A. K. Engstfeld,§ J. Klein, S. Brimaud* and R. J. Behm*

We describe the construction and discuss the performance of a novel combined ultrahigh vacuum (UHV)-electrochemistry set-up, allowing the controlled preparation and structural characterization of complex nanostructured electrode surfaces by high resolution scanning tunnelling microscopy (STM) under UHV conditions on the one hand and, after electrode transfer under clean conditions, electrochemical measurements under continuous, controlled electrolyte mass transport conditions on the other. Electrochemical measurements can be coupled with online product detection, either using an additional collector electrode or by differential electrochemical mass spectrometry (DEMS). The potential of the set-up will be illustrated in two electrocatalytic reactions on complex, but structurally well-defined bimetallic electrode surfaces, O₂ reduction on Pt_xAg_{1-x}/Pt(111) monolayer surface alloys and bulk CO oxidation on Pt monolayer island modified Ru(0001) electrodes. We will particularly demonstrate the importance of structural characterization after the electrochemical measurements for identifying structural modifications induced by the electrochemical environment and thus avoiding misleading conclusions about the structure–activity relationships.

Received 1st September 2016,
Accepted 21st September 2016

DOI: 10.1039/c6cp06051j

www.rsc.org/pccp

1. Introduction

Surface electrochemistry, aiming at fundamental insights into the electrochemistry at the electrified solid–liquid interface by investigating the electrochemical properties of structurally well-defined single-crystalline electrodes, has developed rapidly over the last few decades.¹ In particular the work of Clavilier and co-workers^{2,3} gave access to a variety of structurally well-defined single crystalline working electrodes which can be prepared by procedures such as flame annealing or other techniques that are easily compatible with electrochemical measurements. The so-called Clavilier method is mainly limited to monometallic electrodes, *e.g.*, Pt, Au, Pd, *etc.*, but simple bimetallic structures such as surfaces covered, *e.g.*, by monolayer films of another metal can be prepared by electrodeposition.⁴ The controlled preparation of more complex, nanostructured bimetallic electrodes and other

electrodes, which are interesting, *e.g.*, both for fundamental reasons as well as for application oriented technical reasons, is rarely achieved by this approach, despite the reports on the controlled formation of surface alloys by co-deposition of two metals on a clean monometallic single crystal surface,⁵ or by annealing of bulk alloys⁶ or bimetallic films.⁷ Therefore, already early on researchers tried to combine the flexibility of sample preparation and sample characterization under ultrahigh vacuum (UHV) conditions with electrochemical (EC) measurements. For this purpose they used combined UHV-EC instruments which allowed them to prepare and characterize electrodes under UHV conditions and then transfer them to an electrochemical cell, if possible without contact to air^{8–24} or using techniques to protect the surface during transport through air.^{25–27} These groups could demonstrate in numerous cases that electrode surfaces prepared under UHV conditions exhibited electrochemical characteristics which fully agreed with expectations based on electrochemical measurements on traditionally prepared single crystal electrodes. Furthermore, spectroscopic measurements performed under UHV conditions on electrode surfaces before electrode immersion and/or after electrode emersion were used to gain information on the state of the surface under electrochemical conditions.^{8–12,14–24,28–33}

Despite the enormous progress in ‘non-UHV’ sample preparation and *in situ* surface characterization, including structural characterization by *in situ* scanning tunnelling microscopy

Institute of Surface Chemistry and Catalysis, Ulm University, Albert-Einstein-Allee 47, D-89081 Ulm, Germany. E-mail: sylvain.brimaud@uni-ulm.de, juergen.behm@uni-ulm.de

† Electronic supplementary information (ESI) available. See DOI: 10.1039/c6cp06051j

‡ Present address: Helmholtz Institute Ulm (HIU) Electrochemical Energy Storage, Helmholtzstr. 11, D-89081 Ulm, Germany and Karlsruhe Institute of Technology (KIT), P.O. Box 3640, 76021 Karlsruhe, Germany.

§ Present address: Physics Dept., Technical University of Denmark, Fysikvej 307, Kgs. Lyngby DK-2800, Denmark.

(STM)^{34,35} or *in situ* surface X-ray diffraction^{36,37} as well as chemical *in situ* characterization³⁸ by *in situ* X-ray absorption spectroscopy (XAS)³⁹ or *in situ* vibrational spectroscopy,⁴⁰ there is a large number of cases where *ex situ* sample preparation and characterization under UHV conditions are advantageous. This is either because these samples cannot be prepared in a controlled way otherwise, or surface characterization under UHV conditions is beneficial, *e.g.*, because of higher resolution or simply because it is more easily accessible. This is particularly true for bimetallic samples, where controlled preparation of electrodes with well-defined surface structures is highly demanding.

Based on our interest in the electrochemistry and electrocatalysis of bimetallic electrode surfaces we aimed at developing a UHV-EC system that would allow controlled sample preparation under UHV conditions combined with high resolution STM for surface characterization, in addition to the use of standard spectroscopy techniques for surface characterization. For deriving structure–activity correlations high resolution STM characterization requires atomic resolution with chemical contrast, which has been achieved for numerous UHV prepared bimetallic surfaces,^{41–45} but has been achieved only in very few cases so far by *in situ* STM imaging.⁵ In order to detect the possible changes in the electrode surface structure induced by the electrochemical measurements, *e.g.*, potential induced restructuring, high resolution STM imaging on the emersed electrodes, after the electrochemical measurement, would be highly desirable as well. On the other hand, for electrocatalytic measurements enforced reactant mass transport and defined mass transport conditions are almost inevitable. Since techniques like the rotating disk measurements are hardly compatible with UHV-EC coupling, this means that the electrochemical cell commonly used in UHV-EC systems should be replaced by a flow cell, which in turn leads to more stringent experimental requirements. As an example, hanging meniscus configurations are essentially incompatible with continuous electrolyte flow and thus do not allow for investigation of the electrodes under reaction conditions. Here it should be noted that for stable STM measurements the sample is mostly tightly connected with a specially shaped sample holder, which is also used during the electrochemical measurements. Finally, having experienced the power and potential of *in situ* spectroscopy^{46,47} and *in situ* product detection, *e.g.*, by use of an additional detector electrode as in the rotating ring disk electrode (RRDE) techniques^{48,49} and in the double disk electrode dual thin-layer flow cell approach⁵⁰ or by online differential electrochemical mass spectrometry (DEMS),^{51–54} we would like to include these options also in the present set-up.

In the following we describe in detail a novel and versatile UHV-STM-flow cell set-up developed by our group. It is combined either with an on-line DEMS or an additional detector electrode, allowing for advanced fundamental investigations at the electrified solid–liquid interface on well-defined bimetallic electrodes that had been prepared and characterized under UHV conditions (Section 2). Subsequently, the performance of this instrument and this approach, in general, and in particular the ability to perform electrochemical and electrocatalytic measurements under clean and well-defined conditions, will

be demonstrated in a number of test measurements on a UHV-prepared Pt(111) electrode, including the hydrodynamic properties of the flow cell (Section 3.1). Finally, we will demonstrate the potential of this combined instrument for electrochemical/electrocatalytic studies of structurally well-defined complex nanostructured electrode surfaces using two examples, (i) the oxygen reduction reaction (ORR) on $\text{Pt}_x\text{Ag}_{1-x}/\text{Pt}(111)$ monolayer surface alloys and (ii) bulk CO electro-oxidation on Pt monolayer island modified Ru(0001) $\text{Pt}_{x\text{-ML}}/\text{Ru}(0001)$ electrodes (Section 3.2). Here we will focus on effects produced by a potential-induced restructuring of the electrode surface during the electrochemical measurements, which can lead to incorrect conclusions on the structure–activity relationships of bimetallic electrode surfaces if the actual structure during the electrochemical/electrocatalytic measurements is not known at the same atomic level as the original surface structure prior to these measurements.

2. Experimental

2.1 Overall system characteristics

The combined UHV-STM – flow cell set-up consists of a UHV stainless steel system with standard facilities for sample preparation and characterization and a home-built pocket-size STM for high resolution structural characterization of electrode surfaces, a transfer chamber, which was attached to the main UHV system *via* a gate valve, manipulators for sample transfer between the two chambers, and the flow cell set-up itself. This is illustrated schematically in Fig. 1a. The dual thin-layer flow cell was mounted on a stainless steel tube and could be retracted and sealed off from the transfer chamber *via* a gate valve, or moved into the transfer chamber and brought into contact with the electrode *via* a linear motion drive. The flow cell largely resembles the dual thin-layer flow cell design introduced by Jusys *et al.* earlier,^{52,55} where the working electrode is included in the first compartment and a second compartment can be equipped with an additional electrode, *e.g.*, for electrochemical detection of oxidizable reaction (side) products, or with an interface connecting a small UHV system with a mass spectrometer. The latter allows for online differential electrochemical mass spectrometry (DEMS) measurements under continuous flow conditions. In the following, the individual parts of this set-up will be described in more detail.

The main UHV system (base pressure 1×10^{-10} mbar) has been described in detail elsewhere^{56,57} and will only be briefly introduced. In short, it contains various facilities for sample preparation, including a sputter gun (SPECS, IQE 11/35), a home-built manipulator for sample heating *via* electron bombardment (up to > 1700 K in 15 s), different metal evaporators depending on the type of metal deposited, including a Knudsen cell (Tectra K-Cell, WKC3) for deposition of metals with lower vaporization temperatures such as Ag (Ag 5.0 N, Mateck) and an electron beam evaporator (Omicron EFM-3) for evaporation of metals with high vaporization temperatures (Pt 4N, Goodfellow). An Auger electron spectroscope (AES – Perkin Elmer 10-155) was employed for chemical surface characterization and a quadrupole mass

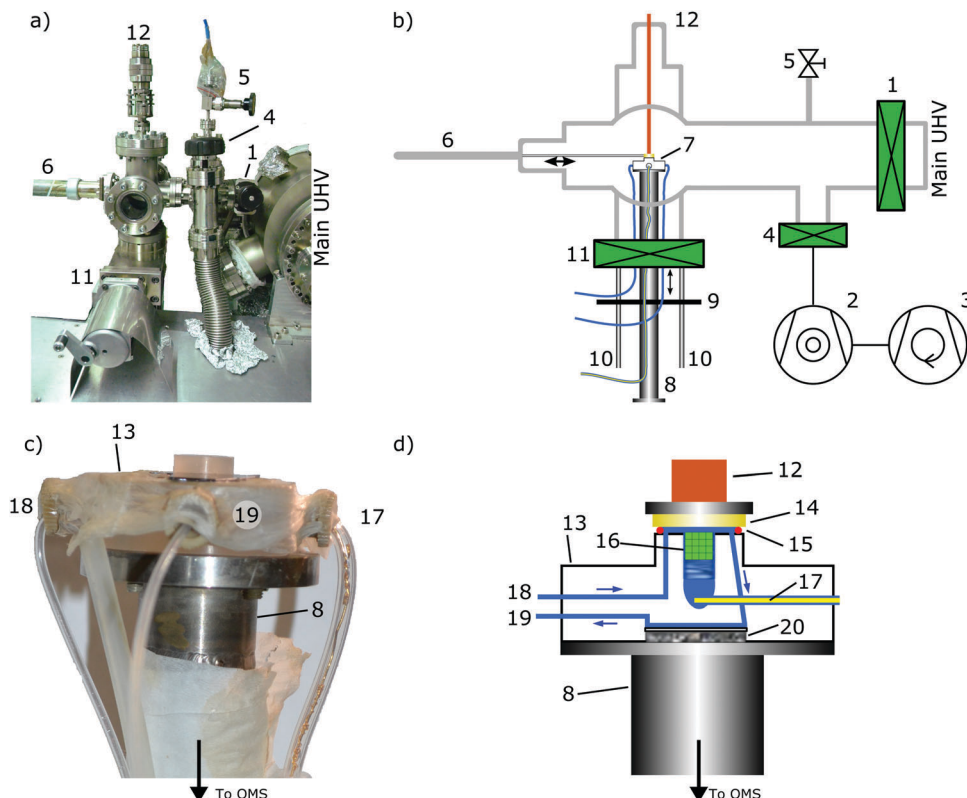


Fig. 1 (a) Photographic and (b) schematic representation of the transfer chamber attached to the main UHV chamber with the electrochemical flow cell set-up, and (c) photographic and (d) detailed schematic representation of the dual thin layer flow cell set-up. Legend: **1**: gate valve between the main UHV chamber and the transfer chamber, **2**: turbomolecular pump (transfer chamber), **3**: roughing pump (transfer chamber), **4**: gate valve protecting the pumps of the transfer chamber, **5**: venting valve, **6**: magnetically coupled linear motion transfer for sample transfer between the main UHV chamber and the transfer chamber, **7**: electrochemical cell, **8**: metal tube connected via flexible bellows to the mass spectrometer chamber, **9**: metal plate holding the tube (**8**), which slides on the steel rods (**10**) via ball bearings mounted in the metal plate, **10**: steel rods serving as guides for the vertical motion of the electrochemical cell, **11**: gate valve separating the transfer chamber from the outside, **12**: electrical feedthrough for contacting the working electrode, **13**: cell body, **14**: working electrode, **15**: O-ring sealing the flow cell during operation, **16**: glass frit between the electrolyte and the counter/reference electrode, **17**: counter electrode, **18**, **19**: inlet and outlet to the flow cell, and **20**: second compartment of the flow cell.

spectrometer (QMS – Balzers QME-125-1) for residual gas analysis. Structural characterization of the electrode surface under UHV conditions was performed using a home-built pocket-size STM. The instrument was sufficiently stable to allow for structural characterization both prior to and after the electrochemical measurements. The tunnelling conditions for the STM measurements are given in the respective figure captions.

2.2 Sample preparation

The single crystals, Pt(111) and Ru(0001) (Mateck GmbH), used for this work are hat shaped with a main diameter of 10 mm and are mounted on a sample holder made of tantalum. For further details on the sample geometry and the sample holder, see ref. 57 and 58. The Pt(111) single crystal was cleaned by Ar^+ sputtering ($\text{HV} = 0.6 \text{ kV}$, $4 \mu\text{A cm}^{-2}$) and subsequent cycles of heating to 1000 K at a rate of 4 K s^{-1} and cooling to RT at a rate of 2 K s^{-1} . During the last cooling-down step, the surface was exposed at 800 K to 10 L of oxygen ($1 \text{ L} = 1.33 \times 10^{-6} \text{ mbar s}$) to remove residual impurities, e.g., carbon, followed by a final heating (to 900 K) and cooling cycle, with identical heating rates mentioned above. $\text{Pt}_x\text{Ag}_{1-x}/\text{Pt}(111)$ surface alloys were prepared by the deposition of

submonolayer amounts of Ag from a Knudsen cell on the freshly prepared Pt(111) surface, followed by annealing of the sample to 900 K with identical heating rates, as mentioned above.

The Ru(0001) single crystal was cleaned by 30 min Ar^+ sputtering ($\text{HV} = 0.7 \text{ kV}$, $4 \mu\text{A cm}^{-2}$) and subsequent exposure to seven cycles of dosing 10 L of oxygen ($1 \text{ L} = 1.33 \times 10^{-6} \text{ mbar s}$, $T_{\text{sample}} < 500 \text{ K}$) and flash annealing ($\sim 15 \text{ s}$) to 1650 K, to remove the remaining carbon impurities. Finally the sample is flash-annealed three times to 1600 K, with 15 min breaks in-between, to desorb the remaining oxygen on the surface originating from oxygen dosing or CO from the previous heating cycles, which had readsorbed during the cool down process after the previous flash annealing cycles. The freshly prepared Ru(0001) single crystal surfaces were modified by Pt via deposition of Pt from an electron beam evaporator on the sample surface at room temperature and subsequent annealing to 750 K, to form compact hexagonally shaped monolayer high Pt islands on the Ru(0001) surface.

2.3 Electrochemical transfer chamber and sample transfer

The electrochemical transfer chamber is shown in Fig. 1a and b in a photograph and in a schematic illustration, respectively.

It consists of a mini UHV chamber (transfer chamber) which is attached to the main UHV chamber by a mechanical gate valve (VAT, Mini UHV valve, **1**). The transfer chamber is pumped by a turbomolecular pump (Pfeiffer, TMU 071P, **2**) with a scroll pump (Varian SH-110, **3**) serving as roughing pump. When the gate valve (**1**) is closed, a base pressure of 5×10^{-8} mbar is reached in the transfer chamber. The pumps can be separated from the transfer chamber by another gate valve (**4**), to protect them from contamination and water vapour when the transfer chamber is vented to atmospheric pressure *via* a venting valve (**5**) (with 6 N N₂, MTI) or exposed to water vapour from the electrochemical cell when inserting the flow cell set-up into the transfer chamber.

The UHV prepared single crystal electrodes can be transported between the transfer chamber and the main UHV chamber by a magnetically coupled linear motion transfer (**6**) equipped with an electrically insulated holder which holds the sample mounted on the tightly connected STM sample holder. The electrochemical cell (**7**) is mounted on a metal tube (**8**), which in turn is held by a metal base plate (**9**). These can be moved vertically by a home-built linear motion drive located at the bottom of the transfer chamber. The vertical motion of the flow cell towards the sample (working electrode) is guided by two steel rods (**10**), which are attached to the gate valve (**11**), and two ball bearings mounted on the metal base plate (**9**). From the top the position of the working electrode can be fixed by a copper rod (**12**), which can be moved vertically by a linear shift and positioned laterally with a port aligner. In combination these allow positioning the working electrode exactly on top of the electrochemical cell, such that perfect sealing between the flow cell and the working electrode is obtained. For electrical contact, the Cu rod is connected with an electrical feed through.

2.4 Electrochemical flow cell

A photograph and a detailed schematic illustration of the electrochemical flow cell are provided in Fig. 1c and d, respectively. The cell body (**13**) is made of Kel-F™ and is mounted on a stainless steel tube (**8**). For the electrochemical characterization of the model electrodes, the sample (**14**) is placed face down on top of the cell body (**13**), where both are separated by an O-ring (**15**) made of a perfluoroelastomer (inner diameter 7 mm, thickness 0.5 mm, FPM, Arcus GmbH), which is situated in a circular groove machined into the cell body. The working electrode (**14**) is pressed from the back side with a copper rod (also used as an electrical contact, **12**) against the O-ring (**15**) on the cell body (**13**) to prevent the leakage of the electrolyte during operation. Furthermore, a glass frit (**16**) is located in the top centre of the cell body, which separates the electrochemical cell compartment from the counter electrode (**17**). The electrolyte enters the cell *via* an inlet (**18**) and leaves the cell *via* an outlet (**19**), leading to the reference electrode (reversible hydrogen electrode, RHE). The electrolyte flows through a first compartment, where the working electrode (**14**) is located, and then to a second compartment (**20**). The direction of the electrolyte flow is indicated by arrows in the schematic illustration in Fig. 1d. The second compartment can either be connected with a mass spectrometer set-up for DEMS

measurements, or equipped with an additional electrode for electrochemical detection of reaction by-products formed at the working electrode. For DEMS measurements, the second compartment (**20**) of the flow cell body is separated from the supporting metal tube (**8**) by a gas permeable membrane supported on a steel frit. The metal tube is connected *via* flexible bellows with another UHV chamber, which contains a differentially pumped quadrupole mass spectrometer (QMS) (Pfeiffer Vacuum QMA 410). This allows for the online detection of volatile species from the electrolyte during the electrochemical characterization of the model electrodes. The DEMS set-up is very similar to the one described in detail elsewhere.⁴⁷ In the second case, the second compartment (**20**) is sealed with a Pt disc, which acts as a current collector for the electrochemical detection of the reaction by-products formed at the working electrode (**14**) in the first compartment, *e.g.*, peroxide detection during ORR measurements. The concept of this novel electrochemical cell is largely inspired by set-ups previously developed in our group for the investigation of high surface area electrodes.^{46,50}

2.5 Electrochemical/electrocatalytic investigations

The electrochemical/electrocatalytic characterization of the model electrodes was performed in 0.5 M H₂SO₄, prepared from H₂SO₄ (Suprapure, Merck) and ultrapure water (MilliQ, 18.2 MΩ cm). Depending on the reactions investigated, the electrolyte was purged with N₂ (6 N, MTI), CO (5 N, Westfalen AG) or O₂ (5.5 N, Westfalen AG). The flow rate of the electrolyte (approximately 2 mL min⁻¹) is driven by the hydrostatic pressure of the electrolyte in the supply bottles, which are located outside the transfer chamber. The electrolyte flows through capillaries (1/16", DuPont® PFA⁺, IDEX) connected to the flow cell. These capillaries are surrounded by additional tubes flushed with N₂ to minimize O₂ diffusion through walls of the capillaries. The electrolyte flow rate can be reduced by decreasing the diameter of the capillary for outflow of the electrolyte during the measurement. A reversible hydrogen electrode (RHE) was employed as a reference electrode, positioned at the outlet of the electrochemical cell. All potentials in this work are related to the RHE scale. The counter-electrode was made of a gold wire (Alfa Aesar, 99.9995%) with additional Au electrodeposited from an Au solution in order to increase the electrochemical surface area. For ORR measurements the potential of the cell is controlled by a bipotentiostat (Pine Instruments, AFCBP-1), which is operated using AfterMath software (Pine Research Instrumentation). For CO electrooxidation measurements we used a potentiostat (Solartron Modulab ECS, model Pstat 1MS/s-2087A), which is operated using Modulab ECS software (Solartron), for potential control. The internal resistances (IR) of the electrochemical cell are compensated externally by connecting the counter and reference electrodes with a capacitor, whose capacitance is chosen depending on the cell configuration and the scan rate (larger capacitors with increasing scan rate). For both potentiostats, IR compensation (ohmic drop) was achieved empirically by comparison of the well-documented Tafel slopes for the ORR and/or the hydrogen evolution reaction kinetics on Pt(111) electrodes reported in the literature (see Section 3.1).

3. Results and discussion

To test the performance and the reliability of the newly designed electrochemical thin-layer flow cell set-up and to avoid misleading conclusions concerning electrochemical features appearing in the electrochemical measurements, which might arise, *e.g.*, from surface contaminants accumulated during the electrode transfer from UHV or from a large internal resistance of the electrochemical cell,⁵⁹ we first performed a number of fundamental measurements on Pt(111) electrodes prepared under UHV conditions (Section 3.1). For these electrodes, the electrochemical and electrocatalytic properties are well documented in the literature. Specifically, we focus on base cyclic voltammetry (CV) in a supporting electrolyte including the hydrogen and hydroxyl electrosorption, the oxygen reduction reaction, and the CO oxidation reaction.

In a second part, we show applications of this combined UHV-STM/electrochemical set-up in structurally complex bimetallic electrodes, which demonstrate the need for high resolution structural characterization of the electrode for a proper understanding of the electrochemical data. This includes the ORR on the $\text{Pt}_x\text{Ag}_{1-x}/\text{Pt}(111)$ surface alloys and the electro-oxidation of CO on Pt modified Ru(0001) surfaces, where the samples were both prepared and structurally characterized by STM under UHV conditions before transferring them to the electrochemical cell (Section 3.2). Rather than presenting a detailed study on these systems, which would be beyond the scope of this paper, we will present some selected experimental results, which allow us to derive an unambiguous relationship between the structural characteristics of the electrode surface and their respective electrocatalytic properties. This will also demonstrate the necessity for structural characterization both before and after the electrochemical measurement, in order to identify the effects induced by restructuring of the electrode surface under (electro-)chemical conditions, an aspect which has been neglected in many if not most studies on model electrodes. These data also illustrate the level of resolution and accuracy that is reachable with this set-up.

3.1. Proof of concept experiments employing a Pt(111) electrode

Clean electrochemical operation. The clean and reproducible operation of the flow cell set-up and the sample transfer is demonstrated by the base CV of a Pt(111) electrode prepared under UHV conditions, which was recorded in 0.5 M H₂SO₄ in a potential range from 0.05 V to 0.85 V (Fig. 2). The base CV shows current features which are characteristic of this electrode and which have been discussed in detail in the literature.^{3,60} In brief, the reversible current features observed in the potential region between 0.05 V and 0.31 V are associated with hydrogen adsorption/desorption (sorption), which overlap at higher potentials between 0.31 V and 0.58 V with characteristic reversible current features associated with (bi)sulphate anion sorption processes. The sharp reversible peaks at 0.45 V are associated with the reorganisation of the (bi)sulphate adlayer.^{61,62} The sharpness of these peaks is not as pronounced as that observed for bead-type Pt(111) electrodes prepared by the Clavilier method and

investigated in a beaker cell,^{60,63} but is still satisfying. The irreversible current features in the potential region between 0.69 V and 0.66 V, attributed to the co-adsorption of hydroxyls,³ are also well resolved. The absence of an additional current peak at 0.12 V, which is considered as characteristic of (110) step sites,^{64,65} is in good agreement with the low step density shown by the representative STM image recorded under UHV conditions prior to the transfer to the electrochemical cell and shown as an inset in Fig. 2. The good quality of the base CV of Pt(111) in the supporting electrolyte convincingly demonstrates the cleanliness of the electrode surface after surface preparation under UHV conditions and the subsequent well-controlled sample transfer from the UHV chamber to the electrochemical cell.

Flow cell characteristics. Next, the performance of the set-up as a flow cell under enforced and controlled electrolyte flow conditions is demonstrated using the O₂ reduction reaction (ORR) on Pt(111) as an example. Potentiodynamic current traces of Pt(111) recorded in O₂ saturated 0.5 M H₂SO₄ at various electrolyte flow rates at a scan rate of 10 mV s⁻¹ are displayed in Fig. 3a (only the positive-going potential scans are displayed). The potentiodynamic current trace can be separated into four potential regions. First, for low overpotentials ($E > 0.80$ V) the oxygen reduction reaction (ORR) is purely kinetically controlled. Second, in the potential region $0.55 \text{ V} < E < 0.80$ V the ORR is controlled by a combination of reactant mass transport limitations and kinetic limitations. Third, in the potential region $0.30 \text{ V} < E < 0.55$ V the reaction rate is solely controlled by the mass transport of the O₂ reactant to the electrode surface. Finally, for potentials < 0.30 V the currents decrease steadily as the electrode potential is decreased. Independent of the electrolyte flow rate, the lowest currents are obtained at 0.05 V. This is associated with increasing H₂O₂ formation, in combination with mass transport limited O₂ supply. On a planar Pt electrode the ORR proceeds *via* a four-electron process in regions one to three, *i.e.*, conversion of O₂ to H₂O dominates, whereas in region four a two-electron process resulting from the conversion of O₂ to H₂O₂ gets more pronounced with decreasing potential,⁶⁶ which in turn results in lower cathodic currents. Overall, these current traces fully agree with examples

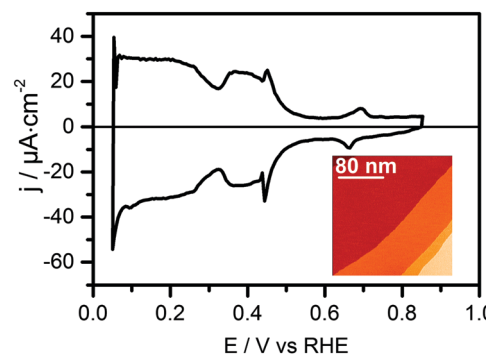


Fig. 2 Base CV of a UHV-prepared Pt(111) electrode recorded in 0.5 M H₂SO₄ (scan rate 50 mV s⁻¹). Inset: Representative large scale STM image (220 nm × 220 nm, $U_t = 900$ mV, $I_t = 4.0$ nA) recorded prior to the transfer to the electrochemical cell.

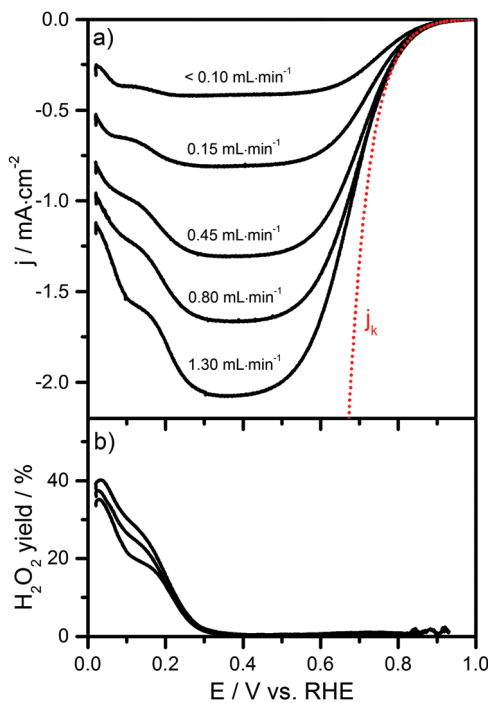


Fig. 3 (a) Total current densities for the ORR on a UHV-prepared Pt(111) electrode recorded in 0.5 M H_2SO_4 (scan rate 10 mV s^{-1}) at different electrolyte flow rates as indicated in the figure (black solid lines) and kinetic current density (red dotted line). (b) Potential dependence of the yield for peroxide formation as derived from the collector current ($E = 1.2$ V).

reported for the ORR on Pt(111) in the O_2 -saturated sulfuric acid electrolyte.^{26,67}

Applying a classical Koutecky-Levich analysis,^{68,69} the Tafel slope and the exchange current density can be determined for the potential-dependent kinetic current density (also shown in Fig. 3a). They were found to be 122 mV dec^{-1} (from 0.90 V to 0.50 V) and $0.5 \times 10^{-4} \text{ mA cm}^{-2}$, respectively. Both values are in good agreement with kinetic data for the ORR on Pt(111) reported previously.⁶⁷

The H_2O_2 produced at high overpotentials, *i.e.*, in region 4 ($E < 0.30$ V), can be detected by a current collector located in the second compartment of the flow cell, which is kept at a constant oxidative potential of $E = 1.20$ V. This set-up, which closely resembles a previous design for a double-disk electrode thin-layer flow cell,⁵⁰ allows us to quantify the fraction of the total current at the Pt(111) electrode arising from the two-electron process by re-oxidation of the resulting H_2O_2 at the collector electrode. The result is shown in Fig. 3b for several electrolyte flow rates. For further analysis the currents resulting from H_2O_2 detection have to be normalized by the flow rate dependent collection efficiency. This was determined before from the ratio of the currents from H_2 evolution at the working electrode and subsequent H_2 oxidation at the collector electrode.⁴⁹ The H_2O_2 yields in the ORR obtained after this normalization⁴⁹ are independent of the electrolyte flow rate. It should be noted that this result is characteristic of massive planar Pt electrodes under low flow conditions, while experiments with nanostructured surfaces, consisting of separate Pt nanostructures,

revealed increasing H_2O_2 yields with increasing flow/decreasing density of the Pt nanostructures (decreasing re-adsorption and further reduction of H_2O_2).⁷⁰ The potential dependence of the H_2O_2 yield follows perfectly the trend given by the total current measured at the Pt(111) electrode (Fig. 3a) and quantitatively agrees with the results of previous RRDE measurements.²⁶ Thus, the dual thin-layer flow cell set-up with a collector electrode developed here provides similar advantages as the rotating ring-disc electrode (RRDE)²⁶ or the double-disk thin-layer flow cell set-ups,^{49,50} which were employed for ORR studies previously, but without direct connection to a UHV system.

The performance of the DEMS detection in combination with the flow cell set-up shall be illustrated by potentiodynamic oxidation of CO on Pt(111) in a CO-free supporting electrolyte and in a CO-saturated supporting electrolyte. The oxidative removal of a saturated CO adlayer (CO_{ad} stripping) on Pt(111) at a scan rate of 10 mV s^{-1} , combined with CO_2 detection by on-line DEMS, was performed after CO adsorption at a constant potential ($E = 0.10$ V) in CO-saturated 0.5 M H_2SO_4 solution, followed by complete removal of the CO dissolved in the electrolyte by rinsing the electrochemical cell for about 40 min with a N_2 purged 0.5 M H_2SO_4 supporting electrolyte. The resulting CO_{ad} stripping voltammogram and the mass spectrometric ion current signal of CO_2 ($m/z = 44$) produced during the reaction are shown in Fig. 4a and b, respectively. During the first positive-going potential scan no current features can be resolved in the potential range between 0.07 V and 0.67 V, indicating complete surface poisoning by adsorbed CO. At *ca.* 0.67 V the CO_{ad} electrooxidation is initiated, followed by a single peak centred at 0.80 V. Both features are also clearly resolved in the CO_2 signal (Fig. 4b). The peak position is in perfect agreement with data reported previously.⁷¹ The absence of a pre-oxidation peak at lower potentials is indicative of a defect-free Pt(111) surface structure,⁷² which in turn agrees fully with our findings of the base CV and STM imaging (see Fig. 2).

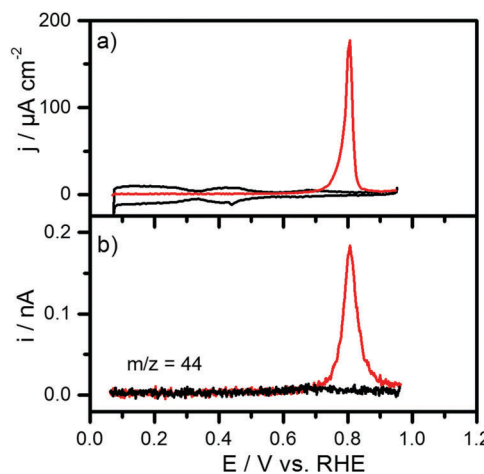


Fig. 4 (a) CO_{ad} stripping voltammogram on Pt(111) in 0.5 M H_2SO_4 (red trace) and subsequent base CV (black trace), (b) $m/z = 44$ ion current (CO_2) detected simultaneously by DEMS during the CO_{ad} stripping experiment (potential scan rate 10 mV s^{-1}).

The second positive-going potential scan, depicted as a black line in Fig. 4a and b, shows the recovery of the current features in the hydrogen region of the Pt(111) electrode. This and the absence of any detectable CO₂ signal in the DEMS signal indicates not only the complete oxidation of the pre-adsorbed CO, but also the successful removal of the dissolved CO in the flow cell set-up. The time-response delay arising from the product mass transport from the electrochemical compartment to the second compartment of the cell, which is interfaced to the mass spectrometer, was in the order of one second, which is significantly faster compared to another set-up also designed for DEMS investigations on single crystal electrodes (not prepared under UHV conditions).⁷³

The current traces for bulk CO electrooxidation on Pt(111) performed in CO saturated 0.5 M H₂SO₄ at 10 mV s⁻¹ and at different electrolyte flow rates are shown in Fig. 5a. The onset potential of the reaction of ca. 0.88 V is shifted by 200 mV towards higher potentials compared to the initiation of the reaction for the CO_{ad} stripping, which is attributed to the higher CO_{ad} coverage achieved in a CO saturated electrolyte than in a CO free electrolyte,⁷⁴ hindering the dissociative adsorption of water molecules on Pt(111).^{75,76} Independent of the electrolyte flow rate, a sharp oxidation peak is located at ca. 0.95 V in the positive-going potential scan, followed by a shoulder at higher potentials. For potentials >0.98 V the reactant mass transport limited current for CO oxidation is reached, which as expected (see below) increases with increasing electrolyte flow rate. The current traces in the negative-going potential scans exhibit a hysteresis, showing a small increase in the current at around 0.92 V (compared to the mass transport limited current for potentials >0.92 V), followed by a continuous decrease of the surface activity for potentials <0.92 V and complete poisoning of the surface by CO_{ad} for potentials <0.82 V. The overall shape of the bulk CO oxidation voltammogram is in good agreement with the results of previous RDE experiments performed on Pt(111).⁷⁷

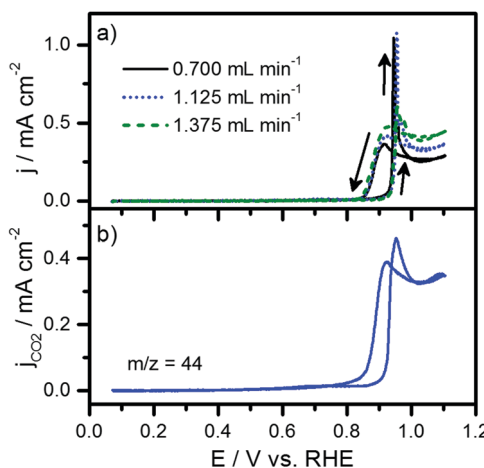


Fig. 5 (a) Faradaic current during bulk CO oxidation on Pt(111) in 0.5 M H₂SO₄ at different electrolyte flow rates as indicated in the figure and (b) partial Faradaic current resulting from the CO₂ ion current recorded during CO oxidation (see text for details) (electrolyte flow rate 1.125 mL min^{-1} , potential scan rate 10 mV s⁻¹).

The CO₂ collection efficiency K^* of the DEMS set-up, which is defined as twice the coulometric charge resulting from the mass spectrometric detection of CO₂ divided by the coulometric charge arising from CO oxidation at a constant potential,^{51,52} was determined from CO oxidation experiments on Pt(111) performed at a constant potential, after having stepped the electrode potential into the potential region where CO mass transport is rate limiting (>0.92 V). This resulted in values in the range of $2.5\text{--}3.5 \times 10^{-5}$, depending on the electrolyte flow rate. These values are of similar order of magnitude as those obtained for an experimental set-up designed for investigations on high surface area electrodes,^{55,78,79} but higher by one order of magnitude than another DEMS set-up specifically designed for experiments with Clavilier's bead-type single crystalline electrodes.⁸⁰ The Faradaic current for CO₂ formation, obtained by normalizing the mass spectrometric CO₂ ion current produced during potentiodynamic bulk CO oxidation with K^* and correction of the time-delay response, is shown in Fig. 5b. The current trace is fully identical to the Faradaic current for bulk CO oxidation shown in Fig. 5a, with CO mass transport limited currents of 0.326 mA cm^{-2} and 0.330 mA cm^{-2} for the former and the latter one, respectively, at an electrolyte flow of 1.125 mL min^{-1} . The absence of a sharp current spike at 0.95 V (see Faradaic current in Fig. 5a) in the mass spectrometric data (Fig. 5b), which in this case is replaced by a much broader hump, can be explained by the broadening of the concentration profile during the electrolyte flow from the working electrode to the second compartment of the flow cell set-up. These features are caused by the rapid oxidation of the adlayer, which can yield rates/currents in excess of the transport limited current.

Finally, the hydrodynamic characteristics of the thin-layer flow cell and the entire set-up were determined from the flow rate dependence of the mass transport limited currents for the ORR and bulk CO electrooxidation. The reactant mass transport limited currents, i_{lim} , for both ORR and bulk CO oxidation are plotted in Fig. 6. Both scale linearly with the square root of the electrolyte flow rate, v , and show an intercept at zero current, in agreement with the modified Levich equation for developing the laminar flow,^{81,82} given as follows:

$$i_{\text{lim}} = 0.68nFCD^{2/3}v^{-1/6}\left(\frac{A}{b}\right)^{1/2}v^{1/2}. \quad (1)$$

This equation relates the transport limited current i_{lim} to the bulk concentration C , the diffusion coefficient D , the working electrode area A , the kinematic viscosity ν of the electrolyte, the number of exchanged electrons n , and the thickness of the electrolyte layer b . The physical situation underlying this equation, with a laminar flow developing parallel to the working electrode, is in good agreement with the design of our electrochemical cell set-up, shown in Fig. 1b, where the electrolyte inlet is located at the periphery of the disc electrode and the electrolyte only starts to develop a laminar flow along the electrode at that point.

The quantitative analysis reveals, however, a limitation arising from the design of the electrochemical flow cell.

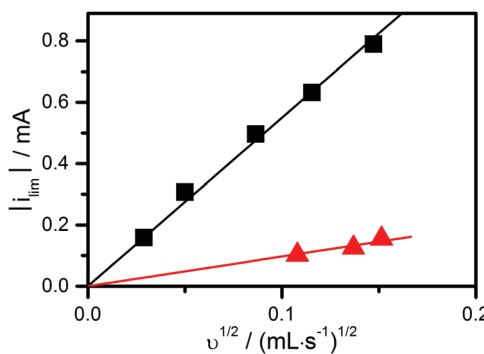


Fig. 6 Plot of the mass transport limited current versus the square root of the electrolyte flow rate for bulk CO oxidation (red triangles) and for the ORR (black squares) on a UHV prepared Pt(111) electrode.

According to eqn (1), and considering that the saturation concentrations and the diffusion coefficients of O₂ and CO in aqueous solution are very similar, the slope of the plot i_{lim} vs. $v^{1/2}$ for the ORR should be twice that of bulk CO electrooxidation (4 electrons exchanged per O₂ molecule in the former reaction vs. 2 electrons exchanged per CO molecule in the latter reaction). As evident from Fig. 6, our experimental results do not match this expectation. This can simply be explained by slight differences in the thickness of the electrolyte layer between the working electrode and the flow cell body (parameter b in eqn (1)), which depends sensitively on the force applied to press the electrode on the tightening O-ring (see Experimental part and Fig. 1). For fixed (volumetric) flow rates this results in different flow velocities in the flow cell, hence in different thicknesses of the diffusion layer and different diffusion rates. These effects, which can lead to variations between different experiments, will modify the mass transport limited currents. They do not affect, however, the analysis of the kinetic currents, where the contribution from the reactant mass transport has been removed (see Section 3.2.1).

Overall, the test measurements on a UHV prepared and structurally well-defined Pt(111) electrode yielded $j(E)$ -curves which fully resemble previous results reported in the literature, illustrating the cleanliness and reproducibility of the sample transfer from the preparation chamber (UHV chamber) to the electrochemical cell and of the sample-cell connection (transfer chamber). Furthermore, these measurements demonstrated the well-defined hydrodynamic properties of the thin-layer flow cell set-up, allowing measurements under well-defined electrolyte mass transport conditions.

3.2. Application to UHV-prepared bimetallic electrodes

In the following section we illustrate the potential of combining high resolution structural characterization by UHV-STM with electrochemical (flow cell) measurements for the mechanistic understanding of electrocatalytic reactions on structurally complex electrode surfaces. We demonstrate that high resolution STM characterization can be performed both before and after the electrochemical measurements. This is particularly important for the understanding of reactions on bimetallic

electrodes, which are sensitive to structural modifications of the surface during the electrochemical measurements. This will be illustrated in two examples: in the first one, O₂ reduction on bimetallic Pt_xAg_{1-x}/Pt(111) monolayer surface alloys, electrochemical etching was indicated by clear modifications of the base CVs. In the second one, bulk CO oxidation on Pt modified Ru(0001) electrodes, the restructuring of the electrode surface is not easily determined from the electrochemical measurements, and thus STM imaging after the electrochemical measurement is even more important for a correct interpretation of the electrochemical data, which is necessary for deriving a correct structure–activity relationship.

3.2.1. ORR on Pt_xAg_{1-x}/Pt(111) surface alloys. In this section we present first the results on the electrochemical properties of structurally well-defined Pt_xAg_{1-x}/Pt(111) monolayer surface alloys in the supporting electrolyte and on the ORR on these electrodes, which illustrate the influence of surface restructuring in some of the samples under electrochemical conditions.

A representative large scale STM image of an as-prepared Pt_xAg_{1-x}/Pt(111) surface alloy (see Fig. 7a) shows atomically flat terraces with monolayer high steps (see also the line scan in Fig. 7b). Identical topographies were found for all surface compositions. The influence of a stepwise increase of the upper potential limit on the voltammetric features in the base CV of two surface alloys, a Pt₆₉Ag₃₁/Pt(111) and a Pt₄₂Ag₅₈/Pt(111) surface alloy recorded in 0.5 M H₂SO₄ is shown in Fig. 7c and d (only the anodic current traces are displayed). These samples can be considered as typical examples for low Ag content and high Ag content surface alloys, respectively. The insets in Fig. 7c and d show atomically resolved STM images with chemical contrast of the respective surfaces taken before the electrochemical measurements (Pt atoms are indicated as brighter spots). They clearly illustrate that the two components in the topmost layer are not randomly distributed, but exhibit a tendency towards phase separation.^{83–85} The current features in the base CV of the Pt_xAg_{1-x}/Pt(111) surface alloys differ significantly in the hydrogen sorption region from the CV associated with the bare Pt(111) electrode (see Section 3.1). The influence of bimetallic Pt–Ag ensembles of surface atoms on the hydrogen adsorption/desorption features was discussed extensively in a separate publication⁸⁵ and shall not be repeated here, since this is not relevant for our further discussion. More important for the present discussion are eventual changes in the current trace in the hydrogen sorption region occurring after potential cycling up to 0.95 V. For the Pt₆₉Ag₃₁/Pt(111) sample with a lower Ag surface content the coulometric charge remains almost constant after a progressive increase of the upper potential limit (Fig. 7c). For the Pt₄₂Ag₅₈/Pt(111) sample with higher Ag surface content, the coulometric charge of the hydrogen region appears to increase with increasing upper potential limit (see Fig. 7d). Changes in the current profile are indicated by arrows. In addition, a small hump in the current trace appears at around 0.50 V. A similar feature was also observed in the CVs recorded on surface alloys with lower amounts of surface Ag (see Fig. 7c).

Considering that hydrogen underpotential deposition current features are not observed for pure Ag electrodes in

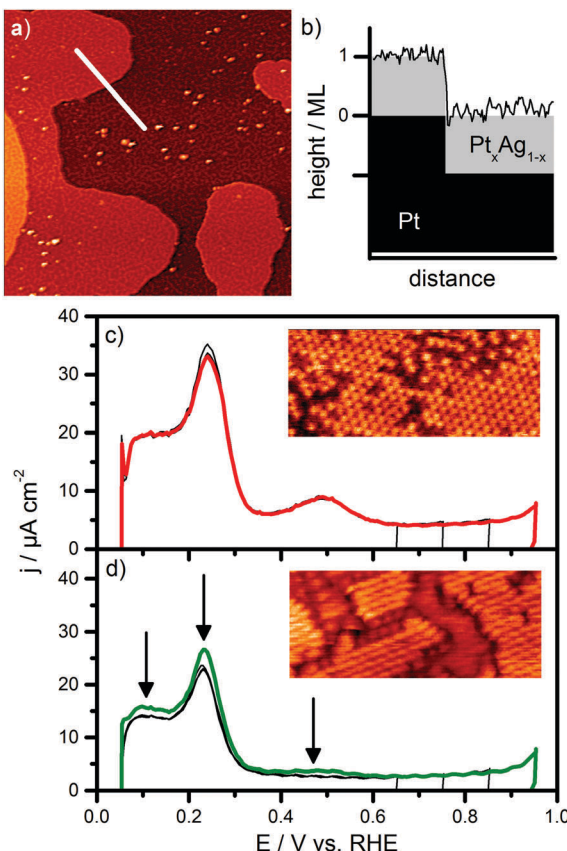


Fig. 7 (a) Representative large scale STM image of an as-prepared $\text{Pt}_x\text{Ag}_{1-x}/\text{Pt}(111)$ monolayer surface alloy before the electrochemical measurement ($270 \text{ nm} \times 270 \text{ nm}$, $U_t = 600 \text{ mV}$, $I_t = 3.2 \text{ nA}$), (b) the corresponding height profile along the line marked in (a) and (c) base CV recorded on a UHV prepared $\text{Pt}_{69}\text{Ag}_{31}/\text{Pt}(111)$ monolayer surface alloy electrode in $0.5 \text{ M H}_2\text{SO}_4$ with increasing upper potential limit (scan rate 50 mV s^{-1}). Inset: Representative atomic resolution STM image before the electrochemical measurements ($12 \text{ nm} \times 5 \text{ nm}$, $U_t = 20 \text{ mV}$, $I_t = 56 \text{ nA}$), (d) base CV recorded on a UHV-prepared $\text{Pt}_{42}\text{Ag}_{58}/\text{Pt}(111)$ monolayer surface alloy electrode in $0.5 \text{ M H}_2\text{SO}_4$ with increasing upper potential limit (at 50 mV s^{-1}). Inset: Representative atomic resolution STM image before the electrochemical measurements ($12 \text{ nm} \times 5 \text{ nm}$, $U_t = 10 \text{ mV}$, $I_t = 28 \text{ nA}$).

acidic electrolytes,⁸⁶ these findings seem to indicate that at high potentials Ag surface atoms in the $\text{Pt}_{42}\text{Ag}_{58}/\text{Pt}(111)$ electrode partly dissolve or form clusters on the surface, which increases the amount of exposed Pt. Such behaviour would not be unexpected, since bulk Ag electrodes are known to be very unstable in acidic electrolytes, with the onset of Ag dissolution at *ca.* 0.50 V .^{86,87}

The ORR on $\text{Pt}_{69}\text{Ag}_{31}/\text{Pt}(111)$ and $\text{Pt}_{42}\text{Ag}_{58}/\text{Pt}(111)$ surface alloys was investigated in O_2 -saturated $0.5 \text{ M H}_2\text{SO}_4$ at 10 mV s^{-1} . The potential dependent kinetic current densities are presented in Fig. 8a. For comparison, this also includes the current trace obtained for a non-modified Pt(111) electrode (current traces for the ORR are given in the ESI†). Both surface alloys exhibit lower overpotentials for the ORR compared to the bare Pt(111) electrode. At 6 mA cm^{-2} the potentials are lowered by 65 mV and 30 mV with respect to Pt(111) for $\text{Pt}_{69}\text{Ag}_{31}/\text{Pt}(111)$ and $\text{Pt}_{42}\text{Ag}_{58}/\text{Pt}(111)$ surface alloys, respectively, indicating that the presence of surface Ag atoms induces a substantial

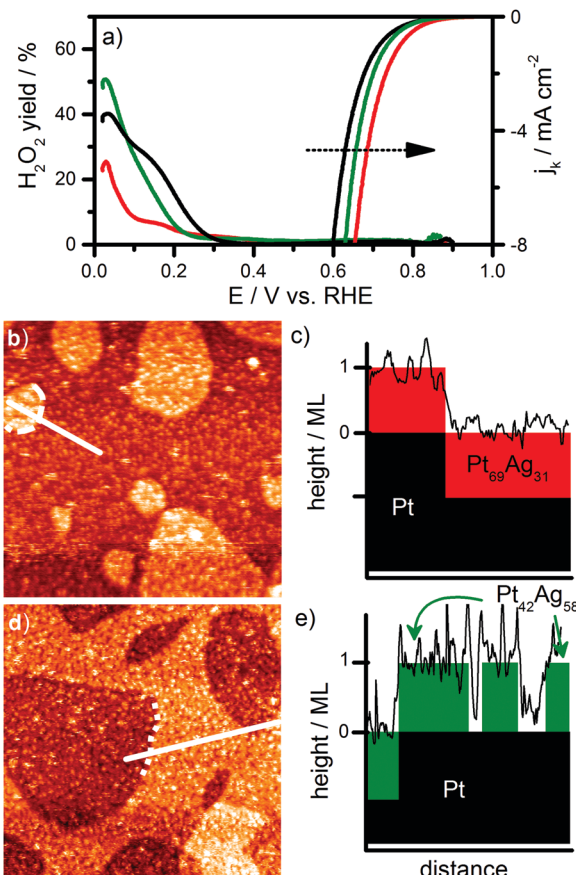


Fig. 8 (a) Kinetic current densities (j_k) and H_2O_2 production yield for the ORR in $0.5 \text{ M H}_2\text{SO}_4$ recorded on Pt(111) (black traces), $\text{Pt}_{69}\text{Ag}_{31}/\text{Pt}(111)$ (red traces) and $\text{Pt}_{42}\text{Ag}_{58}/\text{Pt}(111)$ (green traces) (scan rate 10 mV s^{-1}), (b) representative large scale STM image ($300 \text{ nm} \times 300 \text{ nm}$, $U_t = 100 \text{ mV}$, $I_t = 1.0 \text{ nA}$) recorded on the $\text{Pt}_{69}\text{Ag}_{31}/\text{Pt}(111)$ monolayer surface alloy electrode after the electrochemical measurement, (c) height profile along the line marked in (b), (d) representative large scale STM image ($300 \text{ nm} \times 300 \text{ nm}$, $U_t = 50 \text{ mV}$, $I_t = 6.3 \text{ nA}$) recorded on the $\text{Pt}_{42}\text{Ag}_{58}/\text{Pt}(111)$ monolayer surface alloy electrode after the electrochemical measurement and (e) height profile along the line marked in (d).

enhancement of the ORR activity. Enhanced ORR activities compared to pure Pt samples have been shown in the literature for ill-defined Pt–Ag nanoparticles,^{88–90} but so far not for structurally well-defined planar electrodes.

In addition we also determined the potential-dependent H_2O_2 production yields at high overpotentials (see Fig. 8a). Apparently, they are dramatically influenced by the presence of Ag surface atoms in the monolayer surface alloy.

For more information on the stability and possible corrosive restructuring of the $\text{Pt}_{69}\text{Ag}_{31}/\text{Pt}(111)$ and $\text{Pt}_{42}\text{Ag}_{58}/\text{Pt}(111)$ surface alloys under electrochemical reaction conditions, we performed STM measurements under UHV conditions after the electrochemical measurements. Representative images are displayed in Fig. 8b and d, respectively. The STM images are significantly more noisy than images recorded prior to the electrochemical characterization (see, *e.g.* in Fig. 7a), which we attribute to a higher level of residual adsorbates which remained on the surface after emersion of the sample.⁸⁵ Nevertheless, depending on the

composition of the surface alloy, different structures can be identified by STM imaging before and after the electrochemical characterization. A line profile in the STM image of the Pt₆₉Ag₃₁/Pt(111) sample (Fig. 8b), which is depicted in Fig. 8c reveals a noisy surface level and large monolayer high structures, closely resembling the surface before the electrochemical measurement (see Fig. 7a). This is different for the Pt₄₂Ag₅₈/Pt(111) surface alloy (Fig. 8d), where the line profile in Fig. 8e in addition to the monolayer high structures reveals monolayer deep small holes within the monolayer alloy film. Considering also the changes observed in the base CV of the Pt₄₂Ag₅₈/Pt(111) electrode in Fig. 7d, when the upper potential limit exceeds 0.90 V, we attribute these holes to partial dissolution of Ag from the surface alloy.⁸⁵ While the higher stability of Ag surface atoms compared to bulk Ag can be easily understood from the stabilization of the surface Ag atoms by the underlying Pt(111) substrate, which results in a stronger bonding of the surface Ag atoms compared to pure Ag because of electronic strain and (vertical) ligand effects,^{84,85,91} the different stability of Ag surface atoms in the two surface alloys is more complex and has to be associated with lateral Pt–Ag interactions. This aspect is discussed in more detail elsewhere.⁸⁵

It is important to realize that the ORR measurements were performed on the restructured electrode for the Pt₄₂Ag₅₈/Pt(111) monolayer surface alloy, where restructuring was detected by STM imaging after the electrochemical measurements. These restructuring induced effects are included in the measured current densities, so that the “true” ORR activity of a structurally perfect Pt₄₂Ag₅₈/Pt(111) electrode cannot be measured experimentally. Hence, it is not clear, at least not for surface alloys with higher Ag content (>50%) where corrosive hole formation occurs at potentials exceeding 0.9 V, whether the higher ORR activity of these surfaces is solely or at least mainly due to bimetallic effects including electronic strain and ligand effects and possibly geometrical ensemble effects, or whether structural effects play an important role as well.

These results nicely demonstrate the importance of detailed structural characterization, both before and after electrochemical measurements, in combination with the ability for preparing structurally well-defined electrode surfaces, for the understanding of electrocatalytic reactions on complex bimetallic surfaces. A more detailed report on the ORR activity of Pt_xAg_{1-x}/Pt(111) surface alloys with increasing Ag content is currently under preparation.

3.2.2 Bulk CO electrooxidation on Pt modified Ru(0001) electrodes.

In this second example of structural modifications and, as a result of that, drastic changes in the electrocatalytic properties, we focus on the bulk CO electrooxidation on UHV-prepared Pt island modified Ru(0001) electrodes. Specifically, we will use a Ru(0001) surface modified by monolayer Pt islands with a coverage of 0.3 monolayers (ML) (Pt_{0.3}-ML/Ru(0001)) as an example. STM images of the as-prepared Pt_{0.3}-ML/Ru(0001) surface (Fig. 9a) show a high density of hexagonally shaped Pt islands. Their height of one monolayer is illustrated by the line scan displayed in Fig. 9b. The potentiodynamic current traces for bulk CO electrooxidation performed in CO-saturated

0.5 M H₂SO₄ (scan rate 10 mV s⁻¹) and the CO₂ ion currents detected by DEMS are presented in Fig. 9c and d, respectively, one on an electrode which was exposed before to 40 potential cycles in the pure supporting electrolyte between 0.05 and 0.9 V and one on an electrode which was pre-treated in the same way, but with an upper potential limit of 1.05 V. For comparison, we also included current traces recorded in a similar experiment performed on a bare Pt(111) electrode (see also Fig. 5a and b). For all surfaces there are no current features visible in the potential range between 0 V and 0.55 V, due to blocking of the surface by CO_{ad}, and the reaction is initiated at around 0.55 V (see insets Fig. 9c and d). Even though the base CVs of both Pt_{0.3}-ML/Ru(0001) surfaces show the same current profiles, as described in detail elsewhere,^{92,93} the electrocatalytic activity of these electrodes for potentials >0.55 V depends strongly on the upper potential limit (E_{up}) during the preceding base CVs. If E_{up} was kept in the range up to 0.90 V, the current increases

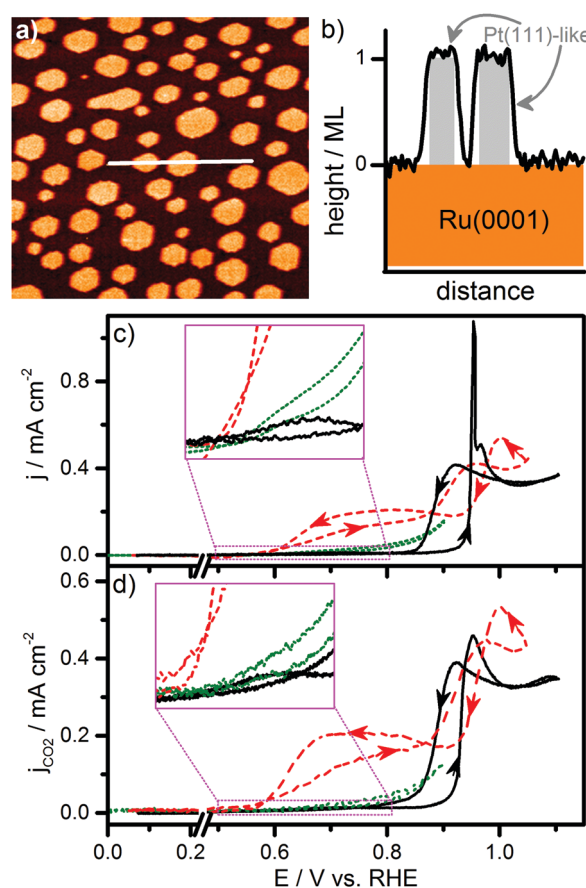


Fig. 9 (a) Representative large area STM image of the as-prepared Pt_{0.3}-ML/Ru(0001) surface before the electrochemical measurements (100 nm × 100 nm, $U_t = 1000$ mV, $I_t = 10$ nA). (b) height profile along the line marked in (a) and (c) potentiodynamic current traces for bulk CO oxidation in 0.5 M H₂SO₄ at 10 mV s⁻¹ for Pt(111) (black trace), Pt_{0.3}-ML/Ru(0001) after potential cycling in a supporting electrolyte (40 cycles) with E_{up} fixed at 0.90 V (green trace) and with E_{up} fixed at 1.05 V (red trace). Arrows indicate the direction of the potential variation. (d) Partial Faradaic currents for CO₂ formation derived from the mass spectrometric CO₂ ion current DEMS signal normalized by the collection efficiency K^* (colours as in c).

smoothly from 0.55 V, reaching a maximum at 0.90 V. In this case the CO oxidation rates are rather similar to those obtained on Pt(111) at potentials between 0.55 V and 0.70 V, while between 0.70 V and 0.90 V the currents are significantly higher on the Pt_{0.3-ML}/Ru(0001) electrode than for Pt(111). On the other hand, when E_{up} was fixed at 1.05 V, the CO oxidation rate was found to increase much faster in the same potential region between 0.55 and 0.90 V than the other two electrodes, reaching a first maximum at ~ 0.80 V and a second higher one at 1.05 V. Hence, the activity of the 1.05 V pre-cycled bimetallic sample clearly exceeds that of the bare Pt(111) electrode in this potential region, and also that of the 0.90 V pre-cycled Pt_{0.3-ML}/Ru(0001) electrode.

The different CO oxidation characteristics of the two Pt_{0.3-ML}/Ru(0001) electrodes can be interpreted by structural differences between the two samples, resulting from their different pre-treatments. A direct proof for that, however, is missing. Likewise, nothing is known about the nature of any possible corrosive restructuring. This information can be obtained from STM imaging after the electrochemical measurements. STM images recorded after two different electrochemical potential cycling pre-treatments are presented in Fig. 10a and c. While after cycling to 0.90 V (Fig. 9c) the surface appears very similar to the as-prepared surface structure with hexagonally shaped monolayer high Pt islands on Ru(0001) (see Fig. 9a), cycling to 1.05 V results in a severe restructuring of the surface (Fig. 10c). The latter image shows dissolution of the Ru(0001) surface as well as multilayer cluster formation. Accordingly, we attribute the enhanced CO oxidation activity of the restructured surface in the potential range of

0.55 and 0.90 V to the newly formed multilayer structures, rather than to Pt–Ru neighbourhoods as expected from the bifunctional effect⁹⁴ (see below). It should be noted that the exact nature and chemical composition of these multilayer structures is still unclear, as they are too rough to be resolved by STM imaging. In such a case further information could be gained from model surfaces with specifically designed nanostructures. This is the subject of current efforts.

Considering that in all cases the reaction is initiated at *ca.* 0.55 V, independently of the electrode structure and composition, it seems that neither the neighbourhood of Ru atoms to supply adsorbed hydroxyls at lower potentials^{94,95} nor the lowering of the CO adsorption energy on Pt by subsurface Ru⁹⁶ influences the first stage of the bulk CO electrooxidation reaction.

In the present example STM imaging after the electrochemical measurements could explain distinct differences in the electrocatalytic behaviour of two bimetallic Pt_{0.3-ML}/Ru(0001) electrodes which were prepared in the same way, but subjected to slightly different potential cycling pre-treatments. Distinct structural differences between both samples could be identified by STM imaging under UHV conditions, which are not apparent in base CVs, most likely because of the very small charge associated with them.

Overall, these two examples demonstrated the unprecedented level of structural detail and accuracy available from such kind of combined UHV-STM – electrochemical flow cell studies. This refers both to the preparation of electrodes with complex, but nevertheless well-defined structure, and to the ability to establishing correlations between (bi)-metallic nanostructures and electrochemical/catalytic properties in terms of structure–activity correlations.

4. Conclusion

We have presented a novel combination of UHV-STM, which allows for controlled sample preparation and structural characterization on an atomic scale, and an electrochemical flow cell set-up. The flow cell allows for electrochemical measurements on these electrodes under controlled electrolyte flow conditions and with the option of simultaneous detection of reactive intermediates/side products or of volatile reaction products by a second electrochemical cell equipped either with an additional electrode or an interface to a mass spectrometer (DEMS). The stability of the UHV-STM and the cleanliness of the sample transfer procedures are sufficient to allow for atomic scale imaging also after electrochemical measurements.

The technical performance of this set-up, in particular of the electrochemical flow cell measurements, was demonstrated by a number of different electrochemical/electrocatalytic measurements on UHV-prepared Pt(111) electrodes. The real potential of this instrument, allowing the preparation of complex nanostructured samples in a reproducible way, the structural characterization of these surfaces on an atomic scale before and after the electrochemical measurement, and clean electrochemical measurements under controlled electrolyte flow conditions,

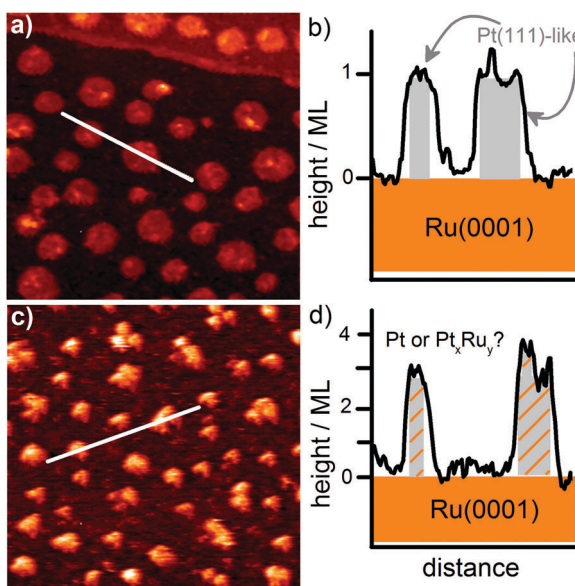


Fig. 10 Representative STM images ($100 \text{ nm} \times 100 \text{ nm}$) of the Pt_{0.3-ML}/Ru(0001) electrode surfaces after the electrochemical measurements (a and c) and the corresponding height profiles (b and d) along the lines marked in (a and c). (a and b) STM image/height profile after electrochemical potential cycling with $E_{\text{up}} = 0.90 \text{ V}$ ($U_t = 100 \text{ mV}$, $I_t = 10 \text{ nA}$), (c and d) STM image/height profile after electrochemical potential cycling with $E_{\text{up}} = 1.05 \text{ V}$ ($U_t = 100 \text{ mV}$, $I_t = 10 \text{ nA}$).

was illustrated in electrocatalytic measurements on two types of bimetallic electrodes, (i) on the ORR on Pt_xAg_{1-x}/Pt(111) monolayer surface alloys and (ii) on the bulk CO oxidation on Pt monolayer island modified Ru(0001) surfaces. Both electrodes were prepared and structurally characterized by STM under UHV conditions. For both cases we find potential induced restructuring of the samples, depending on the surface composition and potential conditions, which results in distinct modifications of the electrochemical and/or electrocatalytic properties, which would hardly be accessible and certainly could not be understood without the sample preparation and structural characterization provided by this instrument. In total, this newly designed set-up is a highly versatile tool for deriving structure-activity-stability correlations on an unprecedented level of structural detail and accuracy.

Acknowledgements

This work was supported by the Deutsche Forschungsgemeinschaft *via* the Research Unit 1376 (project Be 1201/18-2) and the State Foundation of Baden-Württemberg *via* the Competence Network Functional Nanostructures (project B1). AKE is grateful for a fellowship from the “Fond national de la recherche” Luxembourg (grant PHD09-13). We would like to thank H. E. Hoster and O. E. Alves for their contributions in the initial stages of the project.

References

- D. M. Kolb, *Surf. Sci.*, 2002, **500**, 722.
- J. Clavilier, R. Faure, G. Guinet and R. Durand, *J. Electroanal. Chem. Interfacial Electrochem.*, 1980, **107**, 205.
- J. Clavilier, in *Interfacial Electrochemistry, Theory, Experiment and Applications*, ed. A. Wieckowski, Marcel Dekker, New York, 1999, p. 231.
- E. Herrero, L. J. Buller and H. D. Abruña, *Chem. Rev.*, 2001, **101**, 1897.
- F. Maroun, F. Ozanam, O. M. Magnussen and R. J. Behm, *Science*, 2001, **293**, 1811.
- A. M. El-Aziz, R. Hoyer and L. A. Kibler, *ChemPhysChem*, 2010, **11**, 2906.
- Y. Pluntke, L. A. Kibler and D. M. Kolb, *Phys. Chem. Chem. Phys.*, 2008, **10**, 3684.
- W. E. O’Grady, M. Y. C. Woo, P. L. Hagans and E. Yeager, *J. Vac. Sci. Technol.*, 1977, **14**, 365.
- P. N. Ross Jr, *Surf. Sci.*, 1981, **102**, 463.
- E. Yeager, A. Homa, B. D. Cahan and D. Scherson, *J. Vac. Sci. Technol.*, 1982, **20**, 628.
- F. T. Wagner and P. N. Ross, *J. Electroanal. Chem.*, 1983, **150**, 141.
- A. T. Hubbard, J. L. Stickney, M. P. Soriaga, V. K. F. Chia, S. D. Rosasco, B. C. Schardt, T. Solomun, D. Song, J. H. White and A. Wieckohski, *J. Electroanal. Chem. Interfacial Electrochem.*, 1984, **168**, 43.
- P. N. Ross and F. T. Wagner, in *Adv. Electrochem. Electrochem. Eng.*, ed. H. Gerischer and C. W. Tobias, John Wiley & Sons, New York, 1984, vol. 13, p. 69.
- S. Haupt, U. Collisi, H. D. Speckmann and H. H. Strehblow, *J. Electroanal. Chem. Interfacial Electrochem.*, 1985, **194**, 179.
- D. Aberdam, R. Durand, R. Faure and F. EL-Omar, *Surf. Sci.*, 1986, **171**, 303.
- D. M. Kolb, *Z. Phys. Chem.*, 1987, **154**, 179.
- T. Solomun, W. Richtering and H. Gerischer, *Ber. Bunsenges. Phys. Chem.*, 1987, **91**, 412.
- M. Wasberg, L. Palaikis, S. Wallen, M. Kamrath and A. Wieckowski, *J. Electroanal. Chem.*, 1988, **256**, 51.
- L. W. H. Leung, T. W. Gregg and D. W. Goodman, *Rev. Sci. Instrum.*, 1991, **62**, 1857.
- R. L. Borup, D. E. Sauer and E. M. Stuve, *Surf. Sci.*, 1993, **293**, 10.
- G. A. Attard, R. Price and A. Al Akl, *Electrochim. Acta*, 1994, **39**, 1525.
- R. Dalbeck, H. W. Buschmann and W. Vielstich, *J. Electroanal. Chem.*, 1994, **369**, 233.
- W. Chrzanowski and A. Wieckowski, in *Interfacial Electrochemistry. Theory, Experiment, Applications*, ed. A. Wieckowski, Marcel Dekker Inc., New York, 1999, p. 937.
- H. E. Hoster and H. A. Gasteiger, in *Electrocatalysis*, ed. W. Vielstich, H. A. Gasteiger and A. Lamm, Wiley, Chichester, 2003, vol. 2, p. 236.
- H. A. Gasteiger, N. M. Markovic and P. N. Ross, *J. Phys. Chem.*, 1995, **99**, 8945.
- N. M. Markovic, H. A. Gasteiger and P. N. Ross, *J. Phys. Chem.*, 1995, **99**, 3411.
- M. E. Gallagher, C. A. Lucas, V. Stamenkovic, N. M. Markovic and P. N. Ross, *Surf. Sci.*, 2004, **544**, L729.
- W. C. Johnson and L. A. Heldt, *J. Electrochem. Soc.*, 1974, **121**, 34.
- J. S. Hammond and N. Winograd, *J. Electroanal. Chem. Interfacial Electrochem.*, 1977, **80**, 123.
- A. T. Hubbard, J. L. Stickney, S. D. Rosasco, M. P. Soriaga and D. Song, *J. Electroanal. Chem. Interfacial Electrochem.*, 1983, **150**, 165.
- P. M. A. Sherwood, *Chem. Soc. Rev.*, 1985, **14**, 1.
- J. P. Bellier, J. Lecoeur and A. Rousseau, *J. Electroanal. Chem. Interfacial Electrochem.*, 1986, **200**, 55.
- D. Zurawski, M. Wasberg and A. Wieckowski, *J. Phys. Chem.*, 1990, **94**, 2076.
- J. Wiechers, T. Twomey, D. M. Kolb and R. J. Behm, *J. Electroanal. Chem.*, 1988, **248**, 451.
- D. M. Kolb, *Electrochim. Acta*, 2000, **45**, 2387.
- C. A. Lucas, N. M. Markovic and P. N. Ross, *Surf. Sci.*, 1995, **340**, L949.
- C. A. Lucas, N. M. Markovic and P. N. Ross, *Surf. Sci.*, 1999, **425**, L381.
- Spectroelectrochemistry: Theory and Practice*, ed. R. J. Gale, Plenum Press, New York, 2016, p. 1.
- A. E. Russell and A. Rose, *Chem. Rev.*, 2004, **104**, 4613.
- T. Iwasita and F. C. Nart, *Prog. Surf. Sci.*, 1997, **55**, 271.
- M. Schmid, H. Stadler and P. Varga, *Phys. Rev. Lett.*, 1993, **70**, 1441.

- 42 F. Besenbacher, E. Laegsgaard, L. P. Nielsen, L. Ruan and I. Stensgaard, *J. Vac. Sci. Technol., B: Microelectron. Nanometer Struct. – Process., Meas., Phenom.*, 1994, **12**, 1758.
- 43 B. Gleich, M. Ruff and R. J. Behm, *Surf. Sci.*, 1997, **386**, 48.
- 44 F. Buatier de Mongeot, M. Scherer, B. Gleich, E. Kopatzki and R. J. Behm, *Surf. Sci.*, 1998, **411**, 249.
- 45 W. A. Hofer, G. Ritz, W. Hebenstreit, M. Schmid, P. Varga, J. Redinger and R. Podloucky, *Surf. Sci.*, 1998, **405**, L514.
- 46 Y.-X. Chen, M. Heinen, Z. Jusys and R. J. Behm, *Angew. Chem., Int. Ed.*, 2006, **45**, 981.
- 47 M. Heinen, Y. X. Chen, Z. Jusys and R. J. Behm, *Electrochim. Acta*, 2007, **52**, 5634.
- 48 T. J. Schmidt, H. A. Gasteiger and R. J. Behm, *J. Electrochem. Soc.*, 1999, **146**, 1296.
- 49 U. A. Paulus, T. J. Schmidt, H. A. Gasteiger and R. J. Behm, *J. Electroanal. Chem.*, 2001, **495**, 134.
- 50 Z. Jusys, J. Kaiser and R. J. Behm, *Electrochim. Acta*, 2004, **49**, 1297.
- 51 O. Wolter and J. Heitbaum, *Ber. Bunsenges. Phys. Chem.*, 1984, **88**, 2.
- 52 Z. Jusys, H. Massong and H. Baltruschat, *J. Electrochem. Soc.*, 1999, **146**, 1093.
- 53 Z. Jusys, J. Kaiser and R. J. Behm, *Phys. Chem. Chem. Phys.*, 2001, **3**, 4650.
- 54 H. Baltruschat, *J. Am. Soc. Mass Spectrom.*, 2004, **15**, 1693.
- 55 Z. Jusys and R. J. Behm, *J. Phys. Chem. B*, 2001, **105**, 10874.
- 56 E. Kopatzki, S. Günther and W. Nichtl-Pecher, *Surf. Sci.*, 1993, **284**, 154.
- 57 A. Bergbreiter, PhD thesis, Ulm University, 2011, <http://dx.doi.org/10.18725/OPARU-1911>.
- 58 M. Roos, D. Künzel, B. Uhl, H. Huang, O. B. Alves, H. E. Hoster, A. Groß and R. J. Behm, *J. Am. Chem. Soc.*, 2011, **133**, 9208.
- 59 D. van der Vliet, D. S. Strmenik, C. Wang, V. R. Stamenkovic, N. M. Markovic and M. T. M. Koper, *J. Electroanal. Chem.*, 2010, **647**, 29.
- 60 V. Climent, N. Garcia-Araez, E. Herrero and J. Feliu, *Russ. J. Electrochem.*, 2006, **42**, 1145.
- 61 A. M. Funtikov, U. Stimming and R. Vogel, *J. Electroanal. Chem.*, 1997, **428**, 147.
- 62 N. Garcia-Araez, V. Climent, P. Rodriguez and J. M. Feliu, *Langmuir*, 2010, **26**, 12408.
- 63 V. Climent and J. Feliu, *J. Solid State Electrochem.*, 2011, **15**, 1297.
- 64 J. Clavilier, K. El Achi and A. Rodes, *J. Electroanal. Chem.*, 1989, **272**, 253.
- 65 A. Rodes, K. El Achi, M. A. Zamakhchari and J. Clavilier, *J. Electroanal. Chem. Interfacial Electrochem.*, 1990, **284**, 245.
- 66 H. S. Wroblowa, Y.-C. Pan and G. Razumney, *J. Electroanal. Chem.*, 1976, **69**, 195.
- 67 J. X. Wang, N. M. Markovic and R. R. Adzic, *J. Phys. Chem. B*, 2004, **108**, 4127.
- 68 S. Treimer, A. Tang and D. C. Johnson, *Electroanalysis*, 2002, **14**, 165.
- 69 F. J. Vidal-Iglesias, J. Solla-Gullón, V. Montiel and A. Aldaz, *Electrochim. Commun.*, 2012, **15**, 42.
- 70 Y. E. Seidel, A. Schneider, Z. Jusys, B. Wickman, B. Kasemo and R. J. Behm, *Faraday Discuss.*, 2008, **140**, 167.
- 71 L. Palaikis, D. Zurawski, M. Hourani and A. Wieckowski, *Surf. Sci.*, 1988, **199**, 183.
- 72 A. Lopez-Cudero, A. Cuesta and C. Gutiérrez, *J. Electroanal. Chem.*, 2005, **579**, 1.
- 73 A. H. Wonders, T. H. M. Housmans, V. Rosca and M. T. M. Koper, *J. Appl. Electrochem.*, 2006, **36**, 1215.
- 74 R. Gomez and J. M. Feliu, *Electrochim. Acta*, 1998, **44**, 1191.
- 75 S. Gilman, *J. Phys. Chem.*, 1963, **67**, 1989.
- 76 S. Gilman, *J. Phys. Chem.*, 1964, **68**, 70.
- 77 N. M. Markovic and P. N. Ross Jr., *Surf. Sci. Rep.*, 2002, **45**, 117.
- 78 Z. Jusys, J. Kaiser and R. J. Behm, *Langmuir*, 2003, **19**, 6759.
- 79 S. Brimaud, J. Solla-Gullón, I. Weber, J. Feliu and R. J. Behm, *ChemElectroChem*, 2014, **1**, 1075.
- 80 A. E. A. Abd-El-Latif, J. Xu, N. Bogolowski, P. Koenigshoven and H. Baltruschat, *Electroanalysis*, 2012, **3**, 39.
- 81 V. G. Levich, *Physicochemical Hydrodynamics*, Prentice Hall, Eaglewood Cliffs, NJ, 1962.
- 82 J. M. Elbicki, D. M. Morgan and S. G. Weber, *Anal. Chem.*, 1984, **56**, 978.
- 83 H. Röder, R. Schuster, H. Brune and K. Kern, *Phys. Rev. Lett.*, 1993, **71**, 2086.
- 84 R. Rötter, Diploma thesis, Ulm University, 2009.
- 85 S. Beckord, A. K. Engstfeld, S. Brimaud and R. J. Behm, *J. Phys. Chem. C*, 2016, **120**, 16179.
- 86 B. B. Blizanac, P. N. Ross and N. M. Markovic, *Electrochim. Acta*, 2007, **52**, 2264.
- 87 A. Vaskevich, M. Rosenblum and E. Gileadi, *J. Electroanal. Chem.*, 1995, **383**, 167.
- 88 Y. Y. Feng, G. R. Zhang, J. H. Ma, G. Liu and B. Q. Xu, *Phys. Chem. Chem. Phys.*, 2011, **13**, 3863.
- 89 C. L. Lee, Y. J. Chao, C. H. Chen, H. P. Chiou and C. C. Syu, *Int. J. Hydrogen Energy*, 2011, **36**, 15045.
- 90 Y. L. Tsai, K. L. Huang, C. C. Yang, J. S. Ye, L. S. Pan and C. L. Lee, *Int. J. Hydrogen Energy*, 2014, **39**, 5528.
- 91 M. Mavrikakis, B. Hammer and J. K. Nørskov, *Phys. Rev. Lett.*, 1998, **81**, 2819.
- 92 A. K. Engstfeld, S. Brimaud and R. J. Behm, *Angew. Chem., Int. Ed.*, 2014, **53**, 12936.
- 93 A. K. Engstfeld, J. Klein, S. Brimaud and R. J. Behm, *Surf. Sci.*, 2015, **631**, 248.
- 94 M. Watanabe and S. Motoo, *J. Electroanal. Chem.*, 1975, **60**, 275.
- 95 O. A. Petrii, *J. Solid State Electrochem.*, 2008, **12**, 609.
- 96 A. Schlapka, M. Lischka, A. Gross, U. Käsberger and P. Jakob, *Phys. Rev. Lett.*, 2003, **91**, 016101.